Monitoring of Dust Devil Tracks Around the InSight Landing Site, Mars, and Comparison With In Situ Atmospheric Data

C Perrin, S Rodriguez, A Jacob, A Lucas, A Spiga, N Murdoch, R Lorenz, I Daubar, L Pan, T Kawamura, et al.

Geophysical Research Letters

RESEARCH LETTER
10.1029/2020GL087234

Special Section:
InSight at Mars

Monitoring of Dust Devil Tracks Around the InSight Landing Site, Mars, and Comparison With In Situ Atmospheric Data

C. Perrin[1], S. Rodriguez[1,2], A. Jacob[1], A. Lucas[1], A. Spiga[2,3], N. Murdoch[4], R. Lorenz[5], I. J. Daubar[6], L. Pan[7], T. Kawamura[1], P. Lognonné[1,14], D. Banfield[8], M. E. Banks[9], R. F. Garcia[5], C. E. Newman[10], L. Ohja[11], R. Widmer-Schnidrig[12], A. S. McEwen[13], and W. B. Banerdt[14]

[1]Université de Paris, Institut de Physique du Globe de Paris, CNRS, Paris, France, [2]Institut Universitaire de France, Paris, France, [3]Laboratoire de Météorologie Dynamique/Institut Pierre Simon Laplace (LMD/IPSL), Sorbonne Université, Centre National de la Recherche Scientifique (CNRS), École Polytechnique, École Normale Supérieure (ENS), Campus Pierre et Marie Curie BP99, Paris, France, [4]Institut Supérieur de l'Aéronautique et de l'Espace SUPAERO, Toulouse, France, [5]Johns Hopkins University Applied Physics Laboratory, Laurel, MD, USA, [6]Department of Earth, Environmental, and Planetary Sciences, Brown University, Providence, RI, USA, [7]Université de Lyon, Université Claude Bernard Lyon 1, ENS de Lyon, CNRS, UMR 5276 Laboratoire de Géologie de Lyon -Terre, Planètes, Environnement, Villeurbanne, France, [8]Cornell Center for Astrophysics and Planetary Science, Cornell University, Ithaca, NY, USA, [9]NASA Goddard Space Flight Center, Greenbelt, MD, USA, [10]Aeolis Research, Chandler, AZ, USA, [11]Department of Earth and Planetary Sciences, Johns Hopkins University, Baltimore, MD, USA, [12]Black Forest Observatory, Stuttgart University, Wolfach, Germany, [13]Lunar and Planetary Laboratory, University of Arizona, Tucson, AZ, USA, [14]Jet Propulsion Laboratory, California Institute of Technology, Pasadena, CA, USA

Key Points:
- Many fresh linear and dark tracks caused by dust devils are detected from orbit near the InSight landing site
- Dust devil track formation rate decreases in late northern winter then increases in early spring
- Dust devil tracks' azimuths are in good agreement with InSight wind direction measurements

Supporting Information:
- Supporting Information S1

Correspondence to:
C. Perrin,
perrin@ipgp.fr

Citation:
Perrin, C., Rodriguez, S., Jacob, A., Lucas, A., Spiga, A., Murdoch, N., et al. (2020). Monitoring of dust devil tracks around the InSight landing site, Mars, and comparison with in situ atmospheric data. *Geophysical Research Letters*, *47*, e2020GL087234. https://doi.org/10.1029/2020GL087234

Received 5 FEB 2020
Accepted 7 APR 2020
Accepted article online 23 APR 2020

Abstract The NASA InSight mission on Mars is a unique opportunity to study atmospheric processes both from orbit and in situ observations. We use post-landing high-resolution satellite images to monitor dust devil activity during the first 8 months of the mission. We perform mapping and semiautomatic detection of newly formed dust devil tracks and analyze their characteristics (sizes, azimuths, distances, and directions of motion). We find a large number of tracks appearing shortly after landing, followed by a significant decrease of activity during late winter, then a progressive increase during early spring. New tracks are characterized by dark linear, to slightly curvilinear, traces ranging from a few to more than 10 m wide. Tracks are oriented in the ambient wind direction, according to measurements made by InSight's meteorological sensors. The systematic analysis of dust devil tracks is useful to have a better understanding of atmospheric and aeolian activity around InSight.

Plain Language Summary The NASA InSight mission landed on Mars in November 2018. It carries weather and seismic stations that are now working continuously. We are also able to observe the InSight region from orbit using high-resolution satellite images that have been acquired regularly over the first year of the InSight mission. They show a lot of dark traces on the surface, which are caused by whirlwinds called dust devils raising dust into the air. This phenomenon is not observed at the same rate over the entire year, as it depends on atmospheric conditions that vary with season. Our study with satellite images allows us to understand the characteristics of dust devil tracks and compare them with related measurements from the weather station on board InSight. These two sets of observations are well correlated to each other and provide significant constraints to better characterize the atmospheric activity around InSight and in the region of Elysium Planitia, Mars.

1. Introduction

Dust devils form on Earth and Mars when atmospheric convective vortices, resulting from daytime turbulence in the planetary boundary layer, are able to lift dust from the surface. Behind their passage, they usually leave albedo markings, characterized by dark or bright lineaments, called dust devil tracks (DDTs). Even when convective vortices do not carry enough dust particles to make them visible as dust devils, their passage over the surface may lead to tracks, also named DDTs for simplicity.

DDTs have been well documented on Earth and Mars during the last 50 years (e.g., Balme & Greeley, 2006; Reiss et al., 2016, and the references therein). On Mars, successive orbital missions have been able to study dust devils and their associated tracks with ever greater imaging resolution, from Mariner 9 and Viking (e.g., Grant & Schultz, 1987; Thomas & Gierasch, 1985; Veverka, 1976) to Mars Global Surveyor images (e.g., Cantor et al., 2006; Fisher et al., 2005), Mars Express (e.g., Stanzel et al., 2006, 2008), and most recently MRO (Mars Reconnaissance Orbiter) images from the CTX (Context) and HiRISE (High Resolution Imaging Science Experiment) cameras (e.g., Reiss et al., 2014; Verba et al., 2010). In their review, Reiss et al. (2016) classified DDTs into three main families, based on their morphology and albedo contrast with the surrounding surface: dark linear DDTs, bright linear DDTs, and dark cycloidal DDTs. The distinct appearances of tracks result from differing conditions of the atmosphere or properties of the surface dust layer.

The NASA InSight (Interior Exploration using Seismic Investigations, Geodesy and Heat Transport) mission successfully landed in Elysium Planitia (Banerdt et al., 2020; Golombek et al., 2020), carrying the seismometer SEIS (Seismic Experiment for Interior Structure Lognonné et al., 2019) and meteorological instruments through the APSS experiment (Auxiliary Payload Sensor Suite; Banfield et al., 2019; Spiga et al., 2018). Results from APSS have shown intense atmospheric activity at the landing site. In particular, a great number of rapid, short-lived pressure drops occurring between late morning and late afternoon (Banfield et al., 2020), which are diagnostic of a vortex passing over or close to the lander and indicate intense convective vortex activity. Seismic signatures corresponding to convective vortices have also been detected by the SEIS instrument (Kenda et al., 2020; Lognonné et al., 2020; Murdoch et al., 2020). Surprisingly, to date, neither of Insight's cameras (the Instrument Context Camera, ICC, and Instrument Deployment Camera, IDC, located respectively below the deck and on the robotic arm of the InSight lander, Maki et al., 2018) have directly imaged any dust devil, unlike previous missions such as Pathfinder (Ferri et al., 2003), Spirit (Greeley et al., 2006), and Curiosity (Lemmon et al., 2017). Nevertheless, preliminary analysis of ICC images revealed DDTs less than 20 m from the InSight lander (Banerdt et al., 2020). The combination of orbital and InSight images associated with meteorological and seismic data enables the first-ever joint orbital and in situ interpretation of the impact of a convective vortex on a planetary surface. It also enables the improvement of seismic velocity models of the subsurface near InSight (Banerdt et al., 2020; Lognonné et al., 2020).

Reiss and Lorenz (2016) analyzed eight prelanding HiRISE images (25 cm per pixel, McEwen et al., 2007) acquired between March 2010 and February 2014, covering partially a wide area of ~20,000 km^2, corresponding to the four candidate landing sites in Elysium Planitia (Golombek et al., 2014). They did not observe active dust devils directly but identified more than 500 newly formed DDTs in eight study areas, mostly characterized by narrow linear dark tracks (diameter <10 m). In this paper, we examine the evolution of DDTs around the InSight lander over the first 220 sols of the mission (i.e., from December 2018 to July 2019). Thanks to the efforts of the MRO and HiRISE teams, multiple orbital images of the InSight landing site have been acquired repeatedly over time during the first months of the mission. This is a unique opportunity to study the activity of convective vortices, both from orbit and in situ, while seismic, pressure, and wind data are acquired continuously at high frequency and accuracy.

2. Regional Observation of DDTs in the Vicinity of InSight

2.1. Data and Methods

Starting soon after InSight's landing on 26 November 2018, HiRISE images have been acquired periodically to monitor surface changes around the lander due to active aeolian processes, which are potentially detectable by InSight's seismic and meteorological sensors. In this study, we analyze seven HiRISE images (supporting information Table S1) taken on 6 and 11 December (respectively InSight mission Sol 9 and Sol 14; `ESP_057939_1845 and ESP_058005_1845`), 4 and 21 February (respectively Sols 68 and 84; `ESP_058717_1845 and ESP_058928_1845`), 20 March (Sol 111; `ESP_059284_1845`), 6 April (Sol 127; `ESP_059495_1845`), and 8 July (Sol 218; `ESP_060695_1845`). All were taken at the highest HiRISE resolution, that is, a ground sampling of 25 cm per pixel. Red filter (RED) Reduced Data Records (RDRs) images were georeferenced and co-registered relatively to the first image (`ESP_057939_1845` shown in Figure 1a) and projected on the Mars 2000 geographic coordinate system (Seidelmann et al., 2007).

We analyze consecutive images in order to detect new DDTs formed in between image acquisitions. Direct comparison using blinking techniques (i.e., alternate viewing between two scenes) can be used to detect wide and clear tracks but is not effective for detecting the majority of DDTs, especially small tracks with a low albedo contrast. To overcome those limitations, we additionally performed ratios between images

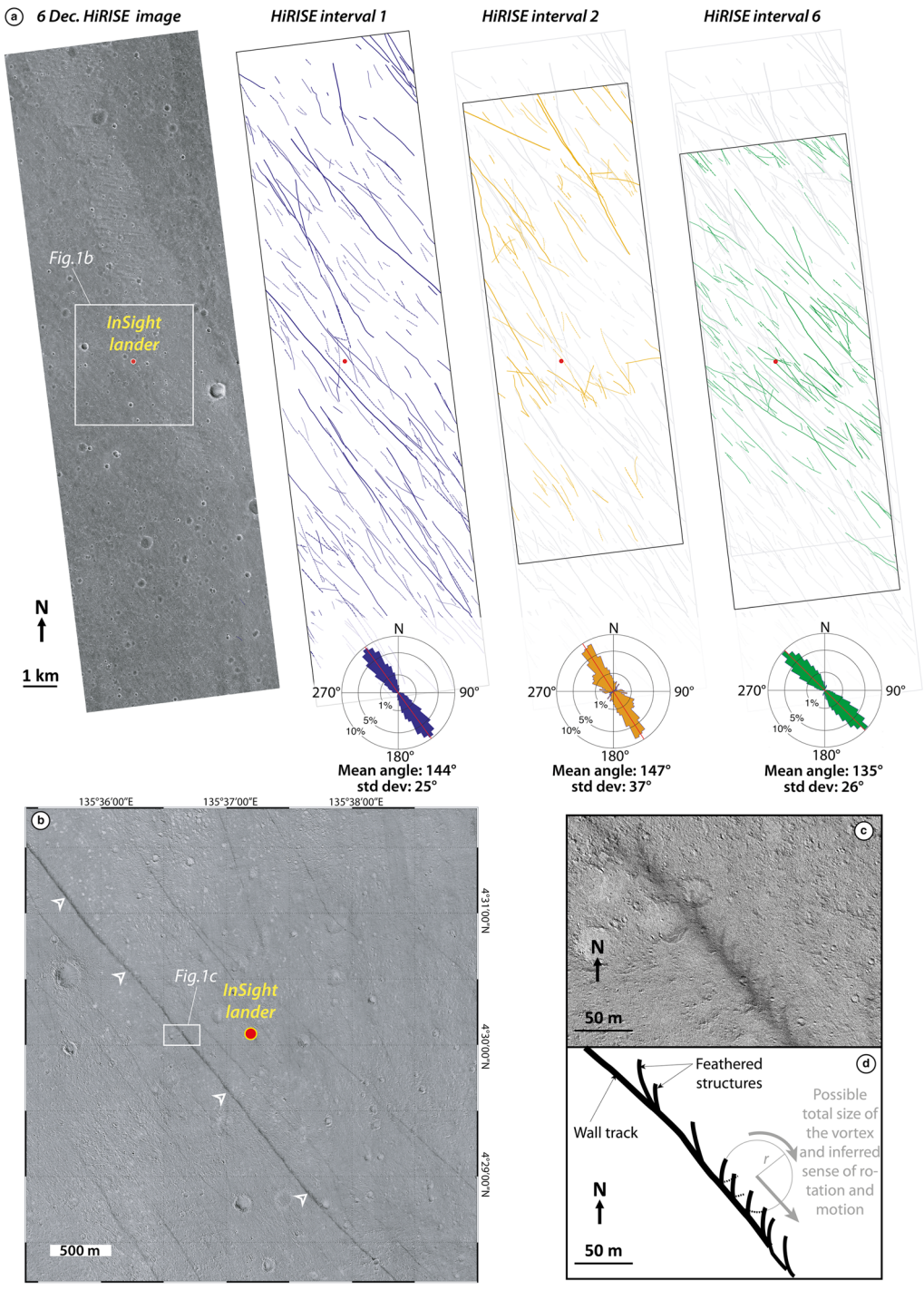

Figure 1. Observation and mapping of dust devil tracks (DDTs) on HiRISE images at the InSight landing site. (a) HiRISE image acquired on 6 December 2018 (ESP_057939_1845_RED RDR) and map of new DDTs manually identified for different periods of time: from 6 to 11 December 2018 (5-sol period, blue lines, HiRISE Interval 1), from 11 December 2018 to 4 February 2019 (54-sol period, orange lines, HiRISE Interval 2), and from 6 April to 8 July 2019 (91-sol period, green lines, HiRISE Interval 6). Gray lines are DDTs identified in the previous time periods. Dashed lines are uncertain DDTs barely seen in ratio images. Black frames surrounding DDTs maps show the overlapping footprint of the successive ratio between HiRISE images. The red dots indicate the InSight lander. Rose diagrams showing the range of DDTs azimuth are presented below each HiRISE interval. Red lines on rose diagrams are mean azimuths. (b) Example ratio image (11 or 6 December 2018) presenting a closer view of new DDTs (dark traces) around the InSight lander. (c, d) Zoom and sketch of the biggest new track observed in December (see white arrows in b). Its feathered structures allow an estimate of the radius (r) of the vortex and its sense of rotation (clockwise) and direction of motion (from the northwest to the southeast). All HiRISE images credit NASA/JPL/University of Arizona.

(i.e., image(t+1)/image(t)) using the raster calculator in the QGIS (Quantum Geographical Information System) software. The ratio images, as is exemplified in Figures 1b and 1c, highlight the surface changes that occurred between the two scenes. The unchanged areas are characterized by a gray faded background where sparse shadowing effects of local relief can be seen (e.g., craters, Figure 1b), due to the different illumination conditions between images. In contrast, surface changes clearly appear with darker or brighter tones in the ratioed images (Figures 1b, 1c, and S1). In particular, new DDTs appear dark in our ratios since vortices remove bright-toned dust to reveal the underlying darker surface. We do not observe new bright DDTs in RDRs images, as were previously reported on Earth and Mars (e.g., Reiss et al., 2011, and the references therein), often found in regions with a thick layer of dust. However, we do observe fading DDTs that appear bright in the ratio images since bright-toned dust depositions occur and the track slowly fades (Figure S1d). In this study, we did not perform measurements of fading rates of DDTs, but previous studies in Gusev Crater have shown that the minimum fading time of a DDT can be up to 211 sols (or 217 terrestrial days; Daubar et al., 2018).

2.2. Manual Mapping and Characteristics of DDTs

Figure 1a presents the regional mapping of the new DDTs identified from both RDRs and ratio images. Detailed analysis of each image has been performed to identify new DDTs in a wide area, up to 100 km^2 (Table S1). Systematic comparison of resulting DDT maps was done in order to ensure that the same DDT was not mapped twice. New DDTs were detected during the following time periods: 6–11 December 2018 (5-sol period, HiRISE Interval 1), 11 December 2018 to 4 February 2019 (54-sol period; HiRISE Interval 2), and 6 April to 8 July 2019 (91-sol period; HiRISE Interval 6). Conversely, no tracks were detected during the following time periods: 4–21 February (16-sol period, HiRISE Interval 3), 21 February to 20 March (27-sol period, HiRISE Interval 4), and 20 March to 6 April (16-sol period, HiRISE Interval 5). This shows a significant seasonal variability of convective vortex activity over almost a terrestrial year, as already pointed out by Verba et al. (2010) based on DDTs detected by HiRISE.

Figure 1a also shows that the highest density of new tracks was observed in the first weeks of the InSight mission, denoting an exceptionally high level of atmospheric activity. Indeed, up to 339 new tracks were mapped in the HiRISE Interval 1, which was only five sols in duration (see blue DDTs in Figure 1a), representing a formation rate as high as 0.68 DDT/sol/km^2. The following longer HiRISE Interval 2 (54 sols) covered by the images was much less active: Only 125 new tracks were mapped (see orange DDTs in Figure 1a), corresponding to a formation rate of 0.03 DDT/sol/km^2, a factor of 20 drop from the first weeks of the InSight mission. Then, after a couple of months in which no tracks were detected (i.e., HiRISE Intervals 3–5), we mapped 213 new tracks (see green DDTs in Figure 1a) that formed during HiRISE Interval 6 (91 sols), corresponding to a formation rate of 0.04 DDT/sol/km^2. These formation rates are gathered in Table S1. We explain in section 4 the caveats of such estimations.

In RDRs and ratio images, new DDTs are characterized by dark linear traces ranging from a few meters to more than 10 m wide (Figures 1 and S1). The along-tracks' lengths range from 40 to 6,770 m (Figure S2), with an average track length of 658 m for complete tracks (i.e., start and end of the DDT visible on the HiRISE image) and >1,347 m for incomplete tracks (i.e., DDTs continue past the edges of the HiRISE footprint) over the three HiRISE intervals considered in Figure 1. These estimates are in good agreement with prelanding measurements made by Reiss and Lorenz (2016). The mean direction of DDTs (180° ambiguity) is persistent over the 8 months, trending mainly NW-SE (Figure 1a; mean direction of all tracks is N138 ±22°E, i.e., measured clockwise from north; see also Figure S3). We note, however, a slight shift in azimuth for the most recent time period (~N135°E, HiRISE Interval 6) compared to the beginning of the mission (~N144°E, HiRISE Interval 1; ~N147°E, HiRISE Interval 2).

We also distinguish locally wider tracks consisting of feathered structures (Figures 1b, 1c, and S1). They correspond generally to "asymmetric" convective vortices (Reiss et al., 2013), which remove dust mainly on one side of their path, creating incomplete cycloidal tracks each made of a wall track and a section of the circular trace of the convective vortex (see Figure 1d). This often occurs when the ratio between ambient wind speed and vortex-induced wind speed is large, which is the case for the time considered here (see section 4). Feathered structures are useful to infer the sense of rotation and direction of motion of the dust devils (Greeley, 2004; Reiss et al., 2016). These feathered tracks are associated with the path of a dust devil, where dust is removed and projected toward the rear of the vortex (solid black lines in Figure 1d). Feathered structures in the front of the dust devil can be distinguished, but they are rapidly faded by the

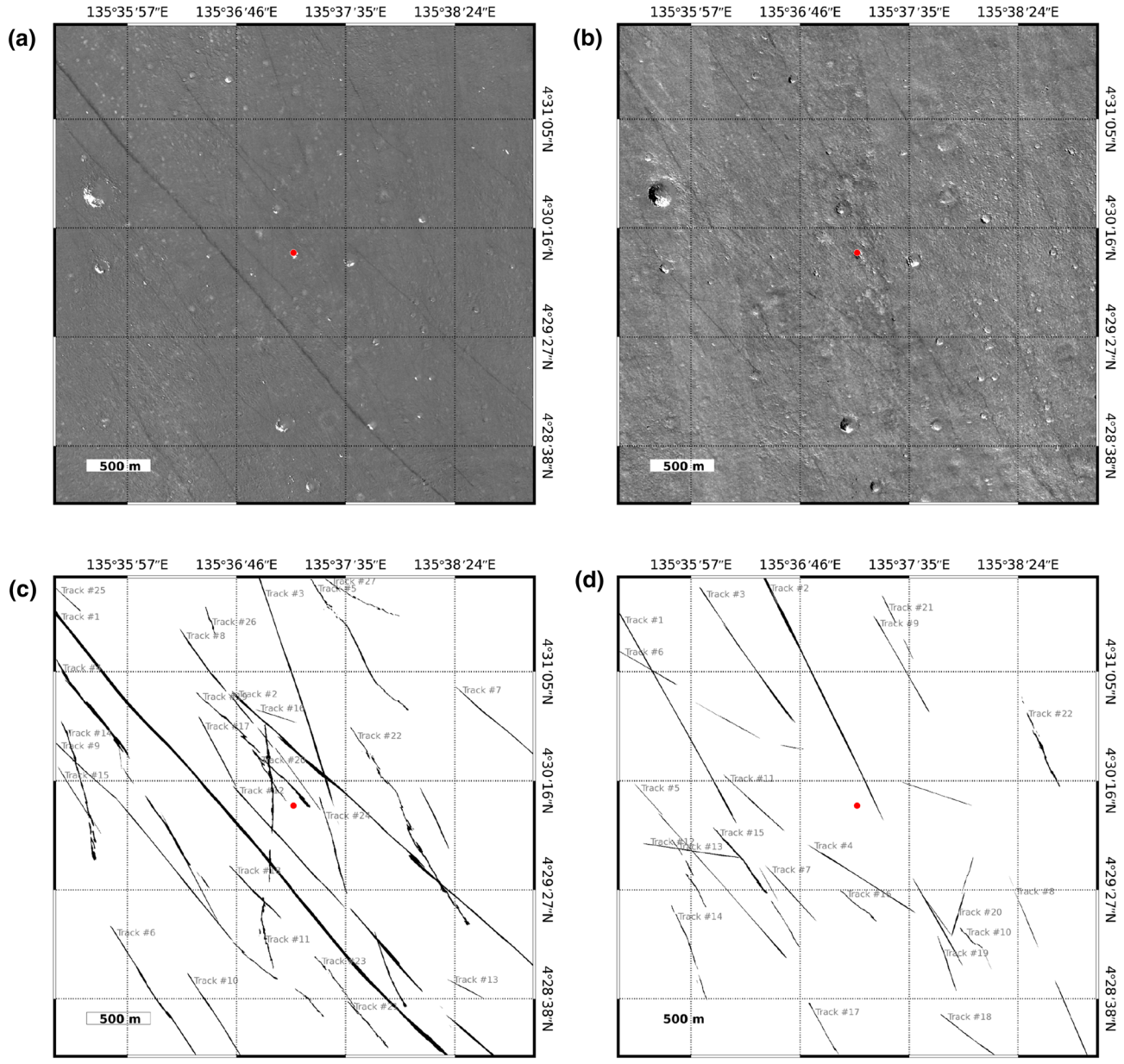

Figure 2. Original ratios (a, b) and DDTs detections using the semiautomated method (c, d) for ratio images during HiRISE Intervals 1 (a, c) and 2 (b, d) (see Table S1). Width, azimuth, and distance of each track relative to the lander are shown in Figure S5.

passage of the vortex (dotted black lines in Figure 1d). Hence, the feathered tracks, only clearly observed in the HiRISE Interval 1 images, indicate both clockwise and counterclockwise rotations of DDTs moving from the NW to the SE (Figures 1b–1d and S1a–S1c). We also observe a single complete cycloidal track a few kilometers north of the lander (Figure S1b) strikingly showing the perfectly circular shape of a convective vortex. We detect only seven new feathered and cycloidal tracks in ratio images and only in HiRISE Interval 1. Based on those feathered tracks, we estimate that the radii r (Figure 1d) of the corresponding vortices range here from 22 to 70 m.

3. Semiautomatic Detection of DDTs

In this section, we compare the manual mapping presented in the previous section with an alternate approach based on a semiautomatic detection of new DDTs in the HiRISE images. This allows us to have an objective analysis of the images and assess the robustness of our mapping. Besides, by focusing on a smaller area around the landing site (square of 12.5 km^2, Figures 1b and 2), the semiautomated detection algorithm

is able to detect new tracks closer to the lander and thus is more representative of the local atmospheric conditions recorded by APSS sensors and potentially detectable by the SEIS instrument.

The semiautomated algorithm to detect DDTs in the ratio images is based on the use of the Radon transform (Toft, 1996), an efficient technique to detect linear or curvilinear features in 2-D images. The main strength of the Radon transform is the ability to extract lines (curves in general) from very noisy images (see method in Figure S4).

Figure 2 presents the ratio images (top) and results of the semiautomatic detection of new DDTs (black lines; bottom) in a ~12.5 km^2 area centered on InSight; 27 new DDTs have been detected in HiRISE Interval 1, while 22 new DDTs have been detected in HiRISE Interval 2, corresponding to a formation rate of ~0.43 and ~0.03 DDTs/sols/km^2, respectively. No new DDTs were found in images in the HiRISE Intervals 3–5. Part of the semiautomatic analysis of new DDTs in the HiRISE Interval 6 can be found in Banerdt et al. (2020).

Our method allows us to extract the trajectory of the DDTs relative to the lander (direction and distance; see Figure S5). As seen in the manual mapping results, the DDTs show a persistent azimuth, ranging from N120°E to N140°E. Most of the DDTs are 8 to 10 m wide (Figure S5), but they can reach tens of meters for larger tracks, averaging their width by considering both the wall track and feathered structures (e.g., ~26 m wide for the feathered track on Figures 1c and S5). In the latter case of a large convective vortex (i.e., diameter >10 m), the DDT's width represents only a lower limit on their size. However, for small convective vortices (i.e., diameter <10 m), the DDT's width can actually be a good estimate of their size. Together with information about DDTs' trajectories, they can be used to calculate expected minimum pressure drops and seismic signals in comparison with InSight measurements (Banerdt et al., 2020; Murdoch et al., 2020).

DDT formation rates deduced from the semiautomatic detection are similar to those obtained from manual mapping: During HiRISE Intervals 1 and 2, 96% and 81% of the DDTs detected by the semiautomatic method are observed in our manual mapping, respectively. Also, the mean azimuth of each track deduced from both methods is in excellent agreement (Figure S6) with a coefficient of determination $R^2 = 0.98$ and 0.99 for HiRISE Intervals 1 and 2, respectively. Since the semiautomatic detection method is more efficient at detecting linear or slightly curvilinear features, more highly curved DDTs are not always detected or are cut into small linear traces, compared to the manual mapping (Figure S7). On the contrary, small low-contrast DDTs are detected by the semiautomatic method but can be hardly visible by eye and thus not considered in the manual mapping (Figure S7). Furthermore, on one hand, the semiautomatic method removes the possible bias of manual mapping, which might consider an interrupted linear track as several individual tracks. On the other hand, the manual mapping can be used as a support to set the threshold of the semiautomatic detection. Both methods are thus complementary and allow us to perform a thorough cross-checking of the information coming from the two analyses to fully characterize the DDTs around InSight.

4. Comparison With InSight Meteorological Measurements and Implications for DDT Formation Rates

Figures 3a–3c present atmospheric measurements from InSight (Temperature and Wind for InSight "TWINS," and pressure, sensors, part of the APSS instrumental suite Banfield et al., 2019; Spiga et al., 2018) since the beginning of the mission up to Sol 220 (10 July 2019), hence covering the range of the analyzed HiRISE images. The mean ambient wind speed and direction are averaged between 8 a.m. and 5 p.m. Local Martian Solar Time, the period during which convective vortices are active according to pressure drop analysis (Banfield et al., 2020). We distinguish three main "APSS stages" in the data:

(i) The first ~50 InSight sols (solar longitude Ls 295–326°) are characterized by a very active atmosphere, with a fairly constant mean daytime wind direction ranging from −40° to −80° (i.e., wind blowing from the NW to the SE according to atmospheric science convention, written asc. below), and high variations of mean wind speed (from 5 to 11 m/s) associated with a large number of pressure drops denoting convective vortices (up to 40 per sol).

(ii) This is followed by a change of meteorological conditions at the InSight landing site, caused by both a large regional dust storm and seasonnal changes (Banfield et al., 2020). This causes the daytime wind direction (Figure 3a) to vary significantly, from −90° (wind blowing from the W) to +120° (wind blowing from the SE), and the mean wind speed to decrease significantly to reach a steady value of about 5 m/s until the decay of the dust storm between Sols 130 and 140 (Ls 8–13°). Convective activity

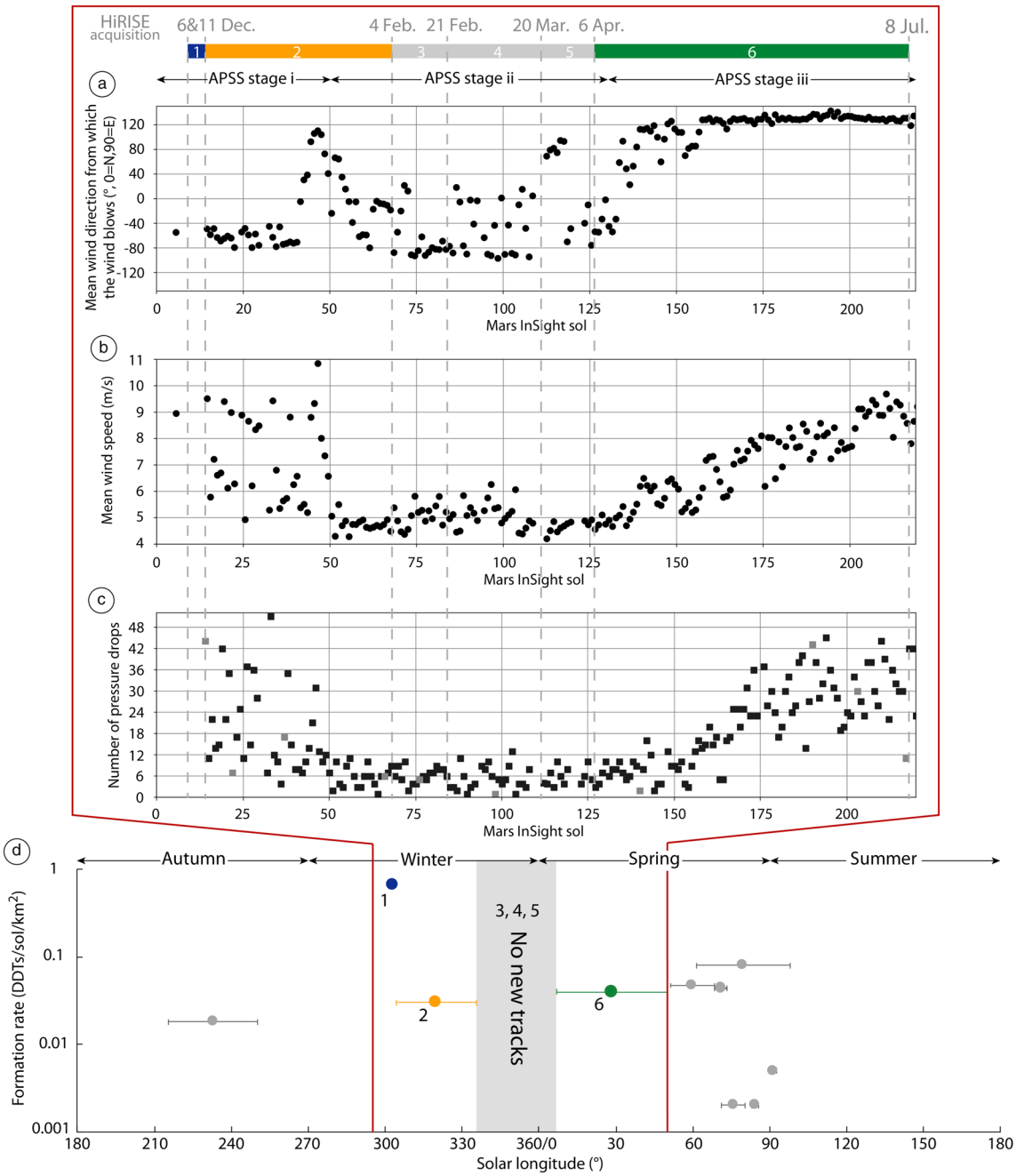

Figure 3. (a) Mean wind direction (shown according to atmospheric science convention; see text for details), (b) mean wind speed, and (c) number of rapid, short-lived pressure drops exceeding 0.3 Pa measured by APSS between sols 0 and 220. Wind measurements are averaged values between 8 a.m. and 5 p.m. LMST (Local Martian Solar Time), corresponding to the time period where convective vortices are active during the Martian day (Banfield et al., 2020). The three different APSS stages are indicated above (see text for details). Colored rectangles correspond to the six HiRISE intervals described in the text (colors similar to Figure 1). The HiRISE acquisition dates (UTC) are indicated by vertical gray dashed lines; (d) DDT formation rates in Elysium Planitia as function of the solar longitude (Ls) from this study (colored dots and gray rectangle) and from Reiss and Lorenz (2016) (gray dots). The red box bounds the 220 sols covered in this study. Seasons in the northern hemisphere are indicated.

is closely linked to both the wind stress at the surface and the surface-to-air temperature difference (e.g., Newman et al., 2019; Rennó et al., 1998). Thus, following the decrease of both ambient wind speed and daytime surface temperature, the number of pressure drops caused by convective vortices also decreases during this stage, ranging from 1 to 12 pressure drops per sol.

(iii) From Sol 130 to Sol 220 (Ls 8–51°), a significant change appears again in the atmospheric activity: The mean wind direction rapidly switched from −40° to +130°, denoting a reversal of the wind direction

from "NW to SE" to "SE to NW." This change in Elysium Planitia was predicted by prelanding climate modeling (Spiga et al., 2018). It occurs at the seasonal transition between northern winter and northern spring. The switch of wind direction is accompanied by a progressively larger increase in mean wind speed and numbers of large pressure drops per sol. Between sols 180 and sols 220, they both reach similar values to the beginning of the mission, but with lower standard deviations.

The regular acquisition of HiRISE images since the beginning of the InSight mission (gray dashed lines in Figure 3) covers the three APSS stages described above. The DDT formation rates deduced from HiRISE images are quite consistent with InSight atmospheric measurements (see also Table S1). The first HiRISE interval (in blue) corresponds to the highest DDT formation rate we measure and also shows the highest atmospheric activity during this time (APSS Stage i). The second HiRISE interval (in orange) covers the transition from high to low atmospheric activity (from APSS Stages i to ii), associated with the regional dust storm during northern winter on Mars. We do observe DDTs during this period, which might have formed in the first part of this interval (i.e., before the transition to APSS Stage ii). Also, the regional dust storm probably affected the surface signature of previously formed DDTs, covering them via dust deposition (Figure S1d). The following third, fourth, and fifth HiRISE intervals (in gray, corresponding to late northern winter season at this location) were quiet in comparison to the other time periods discussed, with respect to both atmospheric conditions (APSS Stage ii) and formation rate of new DDTs. Indeed, we did not detect any new DDTs in HiRISE images during the third, fourth, and fifth intervals. The sixth HiRISE interval (in green) falls within the increase of atmospheric activity during the northern spring (from APSS Stages ii to iii) and also corresponds to the time period during which we do detect new DDTs. This correlation possibly allows us to identify a threshold in the InSight data above which DDTs are formed. The number of pressure drops per sol and wind speed did not exceed 12 and 6 m/s, respectively, during the time periods for which we observe no new DDTs.

The seasonal occurrence of dust devils and their associated tracks was already observed on Mars in other sites than InSight, suggesting also a higher frequency of dust devil formation during local late spring through fall in both the northern and southern hemispheres (Greeley et al., 2006; Reiss et al., 2016; Whelley & Greeley, 2006, 2008). Despite the fact that the HiRISE Intervals 1 and 6 include quiet periods with a low number of large pressure drops (<12 per sol), we do observe new DDTs, implying that they formed mainly during a shorter amount of time when the atmospheric activity was higher (i.e., first half of APSS Stage i and last half of APSS Stage iii, respectively). The DDT formation rates are minimum rates since they strongly depend on the acquisition date of HiRISE images. For an equivalent number of DDTs, the longer the time period between two images (large number of sols), the lower will be the formation rate of DDTs. Moreover, long time periods will favor fading processes of tracks through cumulative dust deposition. This process might hide some tracks formed in the earlier part of the period, artificially lowering the DDTs formation rate. However, we consider that this effect is negligible in our cases, since the time periods between two scenes are all shorter than the fading time ($\leq$ 91 sols, Table S1; Daubar et al., 2018; Reiss & Lorenz, 2016), and most of the DDTs are still observed in the following images. We compare our DDT formation rates with those found by Reiss and Lorenz (2016) in Elysium Planitia (Figure 3d). We find complementary estimates from northern midwinter to midspring (Ls 301° to 50°). Figure 3d completes the overall seasonal variation of the DDT formation rate in Elysium Planitia: It is higher during northern late autumn-early winter (from 0.02 to 0.68 DDTs/sol/km^2) and midspring (~0.05 DDTs/sol/km^2), while a major decrease occurs during both northern late winter and late spring.

Despite the large range of DDT directions measured close to InSight (area in Figure 2) from both methods, their mean directions are in good agreement with the ambient wind directions measured by InSight during the HiRISE intervals where we detected new DDTs (see also Figure S8). The HiRISE Intervals 1, 2, and 6 present a mean azimuth of about N140 $\pm$ 5° E (or −40° asc.) close to the measured mean wind direction during each period and despite the dust storm perturbation (~N120°E, or −60° asc.). Feathered and complete cycloidal tracks were only observed in the first HiRISE interval and confirm that the wind blew from the NW to the SE (Figures 1c and 1d). However, we were not able to deduce such information from DDTs during HiRISE Intervals 2 and 6, due to a lack of feathered and cycloidal tracks. Generally, the mean wind direction value is lower than the mean DDTs direction (Figure S8). HiRISE intervals include large time periods

where the wind activity varies, hence affecting our calculation of the mean direction. For example, during the HiRISE Interval 6 (and APSS Stage iii), InSight recorded an inversion in the wind direction (from SE to the NW). Between Sol 160 and Sol 220, it reaches a steady value of ~N130°E, in better agreement with DDTs directions. This suggests again that DDTs were likely formed during this shorter time period when the atmospheric activity was higher (i.e., last half of APSS Stage iii).

The short time period during the first HiRISE interval might was a chance to compare in more detail with the variation of InSight wind measurements on a timescale of several sols. Unfortunately, at this early stage of the mission, the wind sensors were turned on only for a few hours on 11 December (Figure S9). The measured wind direction at that time shows a fairly constant value of approximately −55° asc., which is slightly different from the direction deduced from the DDTs map (N144°E, or −36° asc.). However, there is an apparent absence of winds coming from −40° asc. (or ~N140°E; Figure S9), surrounded by most of the wind data. This may be due to the wind approaching the TWINS wind sensors from exactly that direction being blocked by the presence of other instruments (the Rotation and Interior Structure Experiment [RISE] and Ultra-High Frequency [UHF] antennas; Banfield et al., 2019). The difference between our DDTs measurements and InSight might come from this unfortunate configuration of instruments on the lander deck.

Previous studies on Earth found a relationship between the standard deviation of DDT migration direction and the ambient wind speed (Figure S10a; Balme et al., 2012, Lorenz, 2016). Under low ambient wind speeds, the DDT is sinuous and random as its path is mainly governed by the internal advection speed of the vortex. As the ambient wind speed increases, the dust devil tends to form a more linear track (Reiss et al., 2016). We cannot assess that this relationship can be linearly applied on Mars (e.g., different wind characteristics, atmospheric pressure, and density). Nevertheless, we do see variations in standard deviation of DDT azimuths and mean ambient wind speed between the different APSS stages. Despite our small data set and the uncertainties, we note a similar trend on Mars as on Earth, showing a decrease of the standard deviation of DDT azimuths as the ambient wind speed increases (Figure S10b). However, we note that all the DDTs mapped in this study are near linear. The regional flat topography of Elysium Planitia might contribute to the formation of linear tracks, even under lower ambient wind speeds. Upcoming acquisition of new orbital images above InSight will allow us to explore this relationship further for Mars.

Studying the characteristics of DDTs is a good indicator of the wind regime measured locally by InSight (Figures 3, S8, and S10). Apart from short-term turbulent fluctuations, the wind is dominated by a combination of global-scale circulations (Hadley cells and thermal tides) and regional contributions (i.e., western boundary currents and moderate slope flows) (Spiga et al., 2018). The wind direction measured by InSight appears to be reasonably steady in the daytime hours (Banfield et al., 2020). Daily variability is also very moderate in the equatorial region where InSight landed; changes of wind direction are mostly seasonal, or driven by rare regional dust storms as occurred around Sol 50 (Banfield et al., 2020).

5. Conclusions

We monitor the activity of convective vortices around InSight on Mars as evinced by their tracks visible in orbital HiRISE images. Manual and semiautomatic detection of DDTs are performed and present similar and complementary results. We observe a large number of dark and linear DDTs in the first days after the InSight landing, followed by a significant decrease and then a progressive increase of their numbers. These observations match the measurements of atmospheric activity obtained by APSS onboard the lander. This behavior correlates well with the transition between seasons on Mars from northern fall, to northern winter and then northern spring. The mean azimuth of DDTs is very persistent (~N138°E), in good agreement with APSS measurements of the mean wind direction. InSight's meteorological data set, with its high-frequency acquisition rates, provides a unique opportunity to conduct DD activity monitoring from both Mars's orbit and surface. The link with APSS data is important because InSight has detected a large number of convective vortices in the pressure and seismic data but surprisingly has imaged no dust devils yet.

Characterization of DDTs is important to better understand seismic, pressure, and wind data signals of passing vortices and to investigate the vortex and ground properties around the InSight lander (Banerdt et al., 2020; Golombek et al., 2020; Murdoch et al., 2020). Future HiRISE images are thus needed to monitor DDTs formation over the summer period around InSight and have a complete overview of atmospheric processes throughout an entire Martian year, in concert with in situ measurements.

Acknowledgments
We thank the HiRISE team for their effort on acquiring new orbital images. All HiRISE images credit NASA/JPL/University of Arizona. Data from APSS and TWINS sensors referenced in this paper are available from the PDS (https://atmos.nmsu.edu/data&urluscore;and&urluscore;services/atmospheres&urluscore;data/INSIGHT/insight.html). We acknowledge NASA, CNES and its partners (UKSA, SSO, DLR, JPL, IPGP-CNRS, ETHZ, IC, and MPS-MPG), and the flight operations team at JPL, CAB, SISMOC, MSDS, IRIS-DMC, and PDS for providing InSight data. Funding support was provided by Agence Nationale de la Recherche (ANR-14-CE36-0012-02 SIMARS and ANR-19-CE31-0008-08 MAGIS). We acknowledge the support of NVIDIA Corporation with the donation of GPU used for this research. This research benefits from the QGIS, an Open Source Geospatial Foundation Project (http://qgis.org). Statistical analysis of DDTs maps has been done using the FracPaQ MATLAB toolbox (Healy et al., 2017). We thank the editor Andrew Dombard and two anonymous reviewers for their constructive comments. This is InSight Contribution Number 124 and IPGP 4130.

References

Balme, M., & Greeley, R. (2006). Dust devils on Earth and Mars. *Reviews of Geophysics*, *44*, RG3003. https://doi.org/10.1029/2005RG000188

Balme, M. R., Pathare, A., Metzger, S. M., Towner, M. C., Lewis, S. R., Spiga, A., et al. (2012). Field measurements of horizontal forward motion velocities of terrestrial dust devils: Towards a proxy for ambient winds on Mars and Earth. *Icarus*, *221*(2), 632–645. https://doi.org/10.1016/j.icarus.2012.08.021

Banerdt, W. B., Smrekar, S. E., Banfield, D., Giardini, D., Golombek, M., Johnson, C. L., et al. (2020). Initial results from the InSight mission on Mars. *Nature Geoscience*, *13*(3), 183–189. https://www.nature.com/articles/s41561-020-0544-y

Banfield, D., Rodriguez-Manfredi, J. A., Russell, C. T., Rowe, K. M., Leneman, D., Lai, H. R., et al. (2019). InSight Auxiliary Payload Sensor Suite (APSS). *Space Science Reviews*, *215*(1), 4.

Banfield, D., Spiga, A., Newman, C., Forget, F., Lemmon, M., Lorenz, R., et al. (2020). The atmosphere of Mars as observed by InSight. *Nature Geoscience*, *13*(3), 190–198. https://www.nature.com/articles/s41561-020-0534-0

Cantor, B. A., Kanak, K. M., & Edgett, K. S. (2006). Mars Orbiter Camera observations of Martian dust devils and their tracks (September 1997 to January 2006) and evaluation of theoretical vortex models. *Journal of Geophysical Research*, *111*, E12002. https://doi.org/10.1029/2006JE002700

Daubar, I. J., Ojha, L., Chojnacki, M., Golombek, M. P., Lorenz, R. D., Wray, J., & Lewis, K. (2018). Lifetime of a dust devil track and dust deposition rate in Gusev Crater. In *49th Lunar and Planetary Science Conference* 19–23 March, 2018, held at The Woodlands, Texas LPI Contribution No. 2083 (1730 pp.).

Ferri, F., Smith, P. H., Lemmon, M., & Rennó, N. O. (2003). Dust devils as observed by Mars Pathfinder. *Journal of Geophysical Research*, *108*(E12), 5133. https://doi.org/10.1029/2000JE001421

Fisher, J. A., Richardson, M. I., Newman, C. E., Szwast, M. A., Graf, C., Basu, S., et al. (2005). A survey of Martian dust devil activity using Mars Global Surveyor Mars Orbiter Camera images. *Journal of Geophysical Research*, *110*, E03004. https://doi.org/10.1029/2003JE002165

Golombek, M., Warner, N. H., Grant, J. A., Hauber, E., Ansan, V., Weitz, C. M., et al. (2020). Geology of the InSight landing site on Mars. *Nature Communications*, *11*(1), 1014. https://www.nature.com/articles/s41467-020-14679-1

Golombek, M. P., Wigton, N., Bloom, C., Schwartz, C., Kannan, S., Kipp, D., et al. (2014). Final four landing sites for the InSight geophysical lander. In *45th Lunar and Planetary Science Conference, held 17–21 March, 2014 at the Woodlands, Texas. LPI contribution no. 1777*, (1499 pp.).

Grant, J. A., & Schultz, P. H. (1987). Possible tornado-like tracks on Mars. *Science*, *237*(4817), 883–885.

Greeley, R. (2004). Martian dust devils: Directions of movement inferred from their tracks. *Geophysical Research Letters*, *31*, L24702. https://doi.org/10.1029/2004GL021599

Greeley, R., Whelley, P. L., Arvidson, R. E., Cabrol, N. A., Foley, D. J., Franklin, B. J., et al. (2006). Active dust devils in Gusev crater, Mars: Observations from the Mars Exploration Rover Spirit. *Journal of Geophysical Research*, *111*, E12S09. https://doi.org/10.1029/2006JE002743

Healy, D., Rizzo, R. E., Cornwell, D. G., Farrell, N. J. C., Watkins, H., Timms, N. E., et al. (2017). FracPaQ: A MATLAB toolbox for the quantification of fracture patterns. *Journal of Structural Geology*, *95*, 1–16.

Kenda, B., Drilleau, M., Garcia, R., Kawamura, T., Murdoch, N., Compaire, N., et al. (2020). Subsurface structure at the InSight landing site from compliance measurements by seismic and meteorological experiments. *Journal of Geophysical Research: Planets*. https://doi.org/10.1029/2020JE006387

Lemmon, M. T., Newman, C. E., Renno, N., Mason, E., Battalio, M., Richardson, M. I., & Kahanpää, H. (2017). Dust devil activity at the Curiosity Mars Rover Field Site. In 48th *Lunar and Planetary Science Conference*, (2952 pp.). The Woodlands, TX.

Lognonné, P., Banerdt, W. B., Giardini, D., Pike, W. T., Christensen, U., Laudet, P., et al. (2019). SEIS: Insight's Seismic Experiment for Internal Structure of Mars. *Space Science Reviews*, *215*(1), 12.

Lognonné, P., Banerdt, W. B., Pike, W. T., Giardini, D., Christensen, U., Garcia, R. F., et al. (2020). Constraints on the shallow elastic and anelastic structure of Mars from InSight seismic data. *Nature Geoscience*, *13*(3), 213–220. https://www.nature.com/articles/s41561-020-0536-y

Lorenz, R. D. (2016). Heuristic estimation of dust devil vortex parameters and trajectories from single-station meteorological observations: Application to InSight at Mars. *Icarus*, *271*, 326–337.

Maki, J. N., Golombek, M. P., Deen, R., Abarca, H., Sorice, C., Goodsall, T., et al. (2018). The color cameras on the InSight lander. *Space Science Reviews*, *214*(6), 105.

McEwen, A. S., Eliason, E. M., Bergstrom, J. W., Bridges, N. T., Hansen, C. J., Delamere, W. A., et al. (2007). Mars Reconnaissance Orbiter's High Resolution Imaging Science Experiment (HiRISE). *Journal of Geophysical Research*, *112*, E05S02. https://doi.org/10.1029/2005JE002605

Murdoch, N., Spiga, A., Lorenz, R. D., Garcia, R. F., Perrin, C., Widmer-Schnidrig, R., et al. (2020). Constraining Martian dust devil vortex and regolith parameters from combined seismic and meteorological measurements. *Journal of Geophysical Research: Planets*. https://doi.org/10.1029/2020JE006410

Newman, C. E., Kahanpää, H., Richardson, M. I., Martínez, G. M., VicenteRetortillo, A., & Lemmon, M. T. (2019). MarsWRF convective vortex and dust devil predictions for Gale Crater over 3 Mars years and comparison with MSLREMS observations. *Journal of Geophysical Research: Planets*, *124*, 3442–3468. https://doi.org/10.1029/2019JE006082

Reiss, D., Fenton, L., Neakrase, L., Zimmerman, M., Statella, T., Whelley, P., et al. (2016). Dust devil tracks. *Space Science Reviews*, *203*(1-4), 143–181. https://link.springer.com/10.1007/s11214-016-0308-6

Reiss, D., & Lorenz, R. D. (2016). Dust devil track survey at Elysium Planitia, Mars: Implications for the InSight landing sites. *Icarus*, *266*, 315–330.

Reiss, D., Raack, J., & Hiesinger, H. (2011). Bright dust devil tracks on Earth: Implications for their formation on Mars. *Icarus*, *211*(1), 917–920.

Reiss, D., Spiga, A., & Erkeling, G. (2014). The horizontal motion of dust devils on Mars derived from CRISM and CTX/HiRISE observations. *Icarus*, *227*, 8–20.

Reiss, D., Zimmerman, M. I., & Lewellen, D. C. (2013). Formation of cycloidal dust devil tracks by redeposition of coarse sands in southern Peru: Implications for Mars. *Earth and Planetary Science Letters*, *383*, 7–15.

Rennó, N. O., Burkett, M. L., & Larkin, M. P. (1998). A simple thermodynamical theory for dust devils. *Journal of the Atmospheric Sciences*, *55*(21), 3244–3252.

Seidelmann, P. K., Archinal, B. A., A'hearn, M. F., Conrad, A., Consolmagno, G. J., Hestroffer, D., et al. (2007). Report of the IAU/IAG Working Group on cartographic coordinates and rotational elements: 2006. *Celestial Mechanics and Dynamical Astronomy*, *98*(3), 155–180. https://link.springer.com/10.1007/s10569-007-9072-y

Spiga, A., Banfield, D., Teanby, N. A., Forget, F., Lucas, A., Kenda, B., et al. (2018). Atmospheric Science with InSight. *Space Science Reviews*, *214*(7), 109. https://link.springer.com/10.1007/s11214-018-0543-0

Stanzel, C., Pätzold, M., Greeley, R., Hauber, E., & Neukum, G. (2006). Dust devils on Mars observed by the High Resolution Stereo Camera. *Geophysical Research Letters*, *33*, L11202. https://doi.org/10.1029/2006GL025816

Stanzel, C., Patzold, M., Williams, D., Whelley, P., Greeley, R., Neukum, G., & The HRSC Co-Investigator Team (2008). Dust devil speeds, directions of motion and general characteristics observed by the Mars Express High Resolution Stereo Camera. *Icarus*, *197*(1), 39–51.

Thomas, P., & Gierasch, P. J. (1985). Dust devils on Mars. *Science*, *230*(4722), 175–177.

Toft, P. (1996). The Radon transform—Theory and Implementation (Ph.D. Thesis). https://backend.orbit.dtu.dk/ws/portalfiles/portal/5529668/Binder1.pdf

Verba, C. A., Geissler, P. E., Titus, T. N., & Waller, D. (2010). Observations from the High Resolution Imaging Science Experiment (HiRISE): Martian dust devils in Gusev and Russell craters. *Journal of Geophysical Research*, *115*, E09002. https://doi.org/10.1029/2009JE003498

Veverka, J. (1976). Variable features on Mars. VII. Dark filamentary markings on Mars. *Icarus*, *27*(4), 495–502.

Whelley, P. L., & Greeley, R. (2006). Latitudinal dependency in dust devil activity on Mars. *Journal of Geophysical Research*, *111*, E10003. https://doi.org/10.1029/2006JE002677

Whelley, P. L., & Greeley, R. (2008). The distribution of dust devil activity on Mars. *Journal of Geophysical Research*, *113*, E07002. https://doi.org/10.1029/2007JE002966